# Multiscale analysis of the particles on demand kinetic model

Ehsan Reyhanian*
*Department of Mechanical and Process Engineering, ETH Zurich, 8092 Zurich, Switzerland*

(Received 23 January 2022; accepted 17 June 2022; published 8 July 2022)

We present a thorough investigation of the particles on demand kinetic model. After a brief introduction of the method, an appropriate multiscale analysis is carried out to derive the hydrodynamic limit of the model. In this analysis, the effect of the time-space dependent comoving reference frames are taken into account. This could be regarded as a generalization of the conventional Chapman-Enskog analysis applied to the lattice Boltzmann models which feature global constant reference frames. Further simulations of target benchmarks provide numerical evidence confirming the theoretical predictions.

DOI: 10.1103/PhysRevE.106.015304

## I. INTRODUCTION

The lattice Boltzmann method (LBM) has developed as an essential tool in computational fluid dynamics [1,2]. The ability of this method in various applications such as multiphase [3–6], micro- [7,8], and turbulent flows [9,10] has long been proven, attracting many researchers to extend the merits of this kinetic-based method. As one of the most fundamental fields in fluid dynamics, compressible flows have been the focus of significant research efforts, leading to development of "gasdynamics." The compressibility of a gas and the thermodynamics of such media allow shock waves and discontinuous solutions, which require special treatments in numerical studies [11].

While the LBM has been extensively used in the incompressible flow regime [1], its application in compressible flows is still an open field of study, directing researchers towards developing various models [12–17]. Considering that the restrictions in the conventional lattice Boltzmann (LB) models are mainly due to the fixed velocity sets [1], the idea of shifted lattices was first introduced in [16], which was found to be significantly useful in increasing the range of performance of LB simulations of supersonic flows [16]. In this method, the peculiar velocities $\boldsymbol{c}_i$ known for each type of lattice [18] are shifted by a constant to mitigate the errors associated with the violation of Galilean invariance

$$\boldsymbol{v}_i = \boldsymbol{c}_i + \boldsymbol{U}. \tag{1}$$

While the model is able to operate well in unilateral flows such as a shock tube, it cannot be used in general setups, where a wide range of temperatures and velocities might emerge. To overcome this, the idea of projecting particles to the comoving reference frame led to the development of the particles on demand kinetic model [19]. In the so-called PonD method, the peculiar velocities are regarded as the relative velocities with respect to the comoving reference frame $\lambda = \{\boldsymbol{u}, T\}$, where $\boldsymbol{u}$ is the local velocity of the flow and $T$ is the local temperature. The new definition of the discrete velocities revokes the known restrictions on the range of velocity and temperature in LBM applications. This opens a novel perspective into the world of computational kinetic methods, especially for simulation of compressible flows. However, in the PonD model, the range of complexity rises as well as its ability to span a wide range of applications, for which the former models were insufficient or computationally nonefficient to provide accurate solutions. For example, with the new realization of the discrete velocities in PonD, the advection becomes nonexact, requiring interpolation techniques, where the accuracy and stability of the model will depend on the choice of interpolation kernels. This is in contrast to the LBM, where a simple and exact point-to-point streaming step is adopted. Therefore, we will carry out a detailed analysis of the model to examine its range of applicability.

In PonD, the discrete velocities are defined as

$$\boldsymbol{v}_i = \sqrt{\theta}\boldsymbol{c}_i + \boldsymbol{u}, \tag{2}$$

where $\theta = T/T_{\mathrm{L}}$ for an ideal gas. Equation (2) describes that the peculiar velocities $\boldsymbol{c}_i$ are first scaled by some definite factor of the square root of the local temperature and then shifted by the local velocity of the flow. While the former revokes the restriction on the lattice temperature $T_{\mathrm{L}}$, the latter results in Galilean invariance. The populations corresponding to the reference frame $\lambda = \{T, \boldsymbol{u}\}$ are denoted by $f_i^{\lambda}$.

## II. EXACT EQUILIBRIUM

To derive the discrete form of the equilibrium, we follow [20] and consider the nondiscrete velocities $\boldsymbol{v} = \sqrt{\theta}\boldsymbol{c} + \boldsymbol{u}$ in the comoving reference frame $\lambda = \{T, \boldsymbol{u}\}$. Upon substitution in the Maxwell-Boltzmann equilibrium function and choosing $\theta = T/T_{\mathrm{L}}$, one gets

$$f^{\lambda,\mathrm{eq}}(\boldsymbol{x}, \boldsymbol{c}) = \frac{\rho}{(2\pi RT)^{D/2}} \exp\left(-\frac{(\boldsymbol{v}-\boldsymbol{u})^2}{2RT}\right) = \frac{\rho}{(2\pi RT)^{D/2}} \exp\left(-\frac{c^2}{2RT_{\mathrm{L}}}\right), \tag{3}$$

*ehsanr@ethz.ch

 

where $D$ stands for the dimension. We define the phase-space integral

$$I = \int \exp\left(-\frac{c^2}{2RT_{\rm L}}\right)\Psi(\boldsymbol{v})d\boldsymbol{v}, \tag{4}$$

where $\Psi$ is a polynomial in $\boldsymbol{v}$. The above integral can be represented by the following series using the Gaussian-type quadrature:

$$I = \sum_{\alpha} W_\alpha \exp\left(-\frac{c_\alpha^2}{2RT_{\rm L}}\right)\Psi(\boldsymbol{v}_\alpha), \tag{5}$$

where $W_\alpha$ are the corresponding weights in each direction $\alpha$. To reduce the computations, it is of interest to consider a one-dimensional case. By using the general definition $\Psi(v) = v^m$, where $m$ is an integer, the integral Eq. (4) becomes

$$I = \sqrt{\theta}\int \exp\left(-\frac{c^2}{2RT_{\rm L}}\right)(\sqrt{\theta}c + u)^m dc. \tag{6}$$

Introducing the scaling factor $\sqrt{2RT_{\rm L}}$ to nondimensionalize the velocity terms, one can rewrite the latter as

$$I = \sqrt{2RT_{\rm L}\theta}^{(m+1)} I_{m,\hat{u}/\sqrt{\theta}}, \tag{7}$$

where

$$I_{m,a} = \int_{-\infty}^{\infty} \exp(-\hat{c}^2)(\hat{c} + a)^m d\hat{c}, \tag{8}$$

and the superscript denotes the dimensionless quantities. It is well known that the following definite integral can be expressed in terms of a third-order Hermite formula

$$I_m = \int_{-\infty}^{\infty} \exp(-x^2)x^m dx = \sum_{j=1}^{3} \tilde{w}_j x_j^m, \tag{9}$$

where $x$ is a dummy variable and $x_1 = -\sqrt{3/2}$, $x_2 = 0$, $x_3 = \sqrt{3/2}$ are the abscissas with the corresponding weights of $\tilde{w}_1 = \sqrt{\pi}/6$, $\tilde{w}_2 = 2\sqrt{\pi}/3$, $\tilde{w}_3 = \sqrt{\pi}/6$. Using the Newton formula, one can expand Eq. (8) as

$$\begin{aligned} I_{m,a} &= \sum_{k=0}^{m}\int_{-\infty}^{\infty} \exp(-x^2)x^m dx \binom{m}{k} a^{m-k} \\ &= \sum_{k=0}^{m}\sum_{j=1}^{3} \tilde{w}_j x_j^k \binom{m}{k} a^{m-k} \\ &= \sum_{j=1}^{3} \tilde{w}_j \sum_{k=0}^{m} x_j^k \binom{m}{k} a^{m-k} \\ &= \sum_{j=1}^{3} \tilde{w}_j (x_j + a)^m. \end{aligned} \tag{10}$$

Therefore, the peculiar discrete velocities are derived as before:

$$\begin{aligned} c_1 &= \sqrt{2RT_{\rm L}}\hat{c}_1 = -\sqrt{3RT_{\rm L}}, \\ c_2 &= 0, \\ c_3 &= \sqrt{2RT_{\rm L}}\hat{c}_3 = \sqrt{3RT_{\rm L}}, \end{aligned} \tag{11}$$

which constructs a $D1Q3$ lattice $\{-C, 0, C\}$ with the lattice temperature $T_{\rm L} = C^2/3$.

Finally, Eq. (7) reduces to

$$\begin{aligned} I &= \sqrt{2RT}\sqrt{2RT_{\rm L}}^m \sum_{i=0}^{3} \tilde{w}_i(\sqrt{\theta}\hat{c}_i + \hat{u})^m \\ &= \sqrt{2\pi RT}\sum_{i=0}^{3} w_i(\sqrt{\theta}c_i + u)^m \\ &= \sqrt{2\pi RT}\sum_{i=0}^{3} w_i \Psi(v_i), \end{aligned} \tag{12}$$

where $w_i = \tilde{w}_i/\sqrt{\pi}$. Due to the splitting property of the phase-space integral, i.e., $d\boldsymbol{c} = dc_1 \cdots dc_D$ the latter formula in $D$ dimensions becomes

$$I = \sqrt{2\pi RT}^D \sum_{\alpha=0}^{\mathcal{Q}} w_\alpha \Psi(v_\alpha), \tag{13}$$

where $w_\alpha = w_{i,j,\ldots,D} = w_i w_j \cdots w_D$ is the tensor product of one-dimensional weights, $v_\alpha = v_{(i,j,\ldots,D)}$ and $\mathcal{Q} = ij\cdots D$ is the total number of discrete velocities. Considering Eq. (5), the Gaussian weights are obtained as

$$W_\alpha = \sqrt{2\pi RT}^D w_\alpha \exp\left(\frac{c_\alpha^2}{2RT_{\rm L}}\right). \tag{14}$$

Finally, the discretized equilibrium populations are derived from the continuous function as

$$\begin{aligned} f_\alpha^{\rm eq} &= W_\alpha f^{\rm eq}(\boldsymbol{x}, c_\alpha) = \sqrt{2\pi RT}^D w_\alpha \exp\left(\frac{c_\alpha^2}{2RT_{\rm L}}\right) \\ &= \sqrt{2\pi RT}^D w_\alpha \exp\left(\frac{c_\alpha^2}{2RT_{\rm L}}\right)\frac{\rho}{(2\pi RT)^{D/2}}\exp\left(-\frac{c_\alpha^2}{2RT_{\rm L}}\right) \\ &= \rho w_\alpha, \end{aligned} \tag{15}$$

which is exact and free of velocity terms and, hence, the Galilean invariance is ensured.

## III. ANALYSIS OF PARTICLES ON DEMAND

In this section, we analyze the kinetic equations in the PonD framework. After a brief introduction of the method, we demonstrate how to derive the recovered thermohydrodynamic limit. Namely, we conduct the Chapman-Enskog analysis by expanding the kinetic equations into multiple levels of time and space scales. Finally, we derive the recovered range of the Prandtl number and present an order verification study.

### A. Kinetic equations

Similar to the LBM, the kinetic equations can split into two main parts. The first is collision using the Bhatnagar-Gross-Krook (BGK) model, with exact equilibrium populations

$$f_i^*(\boldsymbol{x}, t) = f_i(\boldsymbol{x}, t) + \omega(\rho w_i - f_i)_{(\boldsymbol{x},t)}, \tag{16}$$

where $f_i^*(\boldsymbol{x}, t)$ are the postcollision populations, which are computed at the gauge $\lambda = \lambda(\boldsymbol{x}, t)$, and $\omega$ is the relaxation

parameter. Next, the streaming step is conducted via the semi-Lagrangian method, where the information at the monitoring point $(\boldsymbol{x}, t)$ is updated by traveling back through the characteristics to reach the departure point $\boldsymbol{x}_{id} = \boldsymbol{x} - \boldsymbol{v}_i \delta t$. However, due to the dependency of the discrete velocities Eq. (2) on the local flow field, the departure point may be located off the grid points. This is in contrast to the LBM, where the lattice provides exact streaming along the links. Hence, the information at the departure point must be interpolated through the collocation points. Furthermore, in order to be consistent, the populations at the departure point must be in the same reference frame as the monitoring point. Hence, the populations at the collocation points are first transformed to the gauge of the monitoring point and then are interpolated [19]. Finally, the advection step is indicated by

$$f_i(\boldsymbol{x}, t) = \sum_{p=0}^{N-1} \Lambda(\boldsymbol{x}_d - \boldsymbol{x}_p) \mathcal{G}^{\lambda}_{\lambda_p} f^{*\lambda_p}(\boldsymbol{x}_p, t), \tag{17}$$

where $\boldsymbol{x}_p$, $p = 0, \ldots, N-1$, denote the collocation points (grid points) and $\Lambda$ is the interpolation kernel. As mentioned before, the populations are transformed using the transformation matrix $\mathcal{G}$. In general, a set of populations at gauge $\lambda$ can be transformed to another gauge $\lambda'$ by matching $Q$ linearly independent moments:

$$\boldsymbol{M}^{\lambda}_{mn} = \sum_{i=1}^{Q} f_i^{\lambda} v_{ix}^m v_{iy}^n, \tag{18}$$

where $m$ and $n$ are integers. This may be written in the matrix product form as $\boldsymbol{M}^{\lambda} = \mathcal{M}_{\lambda} f^{\lambda}$ where $\mathcal{M}$ is the $Q \times Q$ linear map. Requiring that the moments must be independent from the choice of the reference frame leads to the matching condition

$$\mathcal{M}_{\lambda'} f^{\lambda'} = \mathcal{M}_{\lambda} f^{\lambda}, \tag{19}$$

which yields the transformed populations:

$$f^{\lambda'} = \mathcal{G}^{\lambda'}_{\lambda} f^{\lambda} = \mathcal{M}^{-1}_{\lambda'} \mathcal{M}_{\lambda} f^{\lambda}. \tag{20}$$

Finally, the macroscopic values are evaluated by taking the pertinent moments

$$\rho = \sum_i f_i, \tag{21}$$

$$\rho \boldsymbol{u} = \sum_i f_i \boldsymbol{v}_i, \tag{22}$$

$$\rho u^2 + D\rho T = \sum_i f_i v_i^2. \tag{23}$$

The implicitness in the above equations requires a predictor-corrector step to find the comoving reference frame. Hence, the advection step is repeated by imposing the new evaluated velocity and temperature until the convergence is achieved. To this end, discrete velocities Eq. (2) at each monitoring point $(\boldsymbol{x}, t)$ are initially set relative to the gauge $\lambda_0 = \{T_0, \boldsymbol{u}_0\}$, where $\boldsymbol{u}_0 = \boldsymbol{u}(\boldsymbol{x}, t - \delta t)$ and $T_0 = T(\boldsymbol{x}, t - \delta t)$ are known from the previous time step. Constructing the initial discrete velocities $v_i^0 = \sqrt{\theta_0}\boldsymbol{c}_i + \boldsymbol{u}_0$, the advection Eq. (17) is followed to compute the populations $f_i^{\lambda_0}(\boldsymbol{x})$. Using Eqs. (21)–(23), the new macroscopic quantities are evaluated to define the corrected gauge $\lambda_1 = \{T_1, \boldsymbol{u}_1\}$, which results in the corrected velocities $v_i^1$ and consequent populations $f_i^{\lambda_1}$. The iterations will continue until the reference frame is converged to a fixed value $\lambda_\infty = \lim_{n\to\infty}\{T_n, \boldsymbol{u}_n\}$. In the limit of the comoving reference frame, the computed velocity $\boldsymbol{u}_\infty = \boldsymbol{u}(\boldsymbol{x}, t)$ and temperature $T_\infty = T(\boldsymbol{x}, t)$ by moments Eqs. (22) and (23) are equal to those defined as the reference frame $\lambda_\infty = \lambda(\boldsymbol{x}, t) = \{T(\boldsymbol{x}, t), \boldsymbol{u}(\boldsymbol{x}, t)\}$, i.e.,

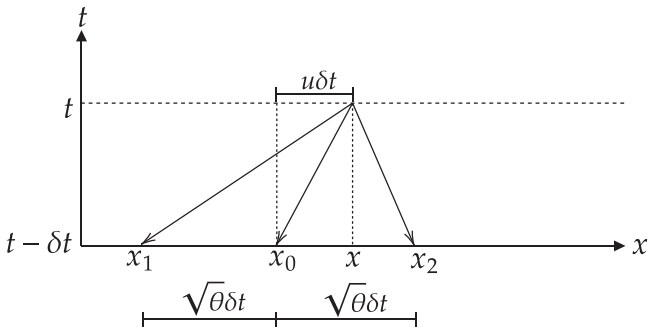


FIG. 1. Schematic of the semi-Lagrangian advection and the location of the departure points.

$$\sum_i f_i^{\lambda} \boldsymbol{u} = \sum_i f_i^{\lambda} (\sqrt{T/T_{\mathrm{L}}} \boldsymbol{c}_i + \boldsymbol{u}), \tag{24}$$

$$\sum_i f_i^{\lambda} (u^2 + DT) = \sum_i f_i^{\lambda} ||\sqrt{T/T_{\mathrm{L}}} \boldsymbol{c}_i + \boldsymbol{u}||^2. \tag{25}$$

For more details, see [19]. A convergence analysis for the iterative algorithm of "predictor-corrector" is provided in the Appendix.

### B. Chapman-Enskog analysis

In this section, we aim at recovering the hydrodynamic limit of the model. Before we begin, it is important to note that due to time-space dependent discrete velocities, the noncommutativity relation $v_{i\alpha}\partial_\alpha f_i \neq \partial_\alpha (v_{i\alpha} f_i)$ is taken into account at each step of the following analysis.

We assume that the comoving reference frame $\lambda(\boldsymbol{x}, t)$ has been reached at the monitoring point. In other words, Eqs. (24) and (25) are legitimate. For simplicity, we first neglect the interpolation process and recast the advection equation as

$$f_i^{\lambda}(\boldsymbol{x}, t) = \mathcal{G}^{\lambda}_{\lambda_i} f_i^*(\boldsymbol{x}_{id}, t - \delta t), \tag{26}$$

where $\lambda_i = \lambda(\boldsymbol{x}_{id}, t - \delta t)$ is the corresponding comoving reference frame at each departure point. Figure 1 illustrates the semi-Lagrangian advection and the departure points using the $D1Q3$ lattice. By definition, Eq. (26) is recast into the following form:

$$f_i^{\lambda}(\boldsymbol{x}, t) = \mathcal{M}^{-1}_{i,\lambda} M^*(\boldsymbol{x}_{id}, t - \delta t), \tag{27}$$

where the dummy indices are dropped in the right-hand side and

$$M^* = \mathcal{M} f^* = M + \omega(M^{\mathrm{eq}} - M) \tag{28}$$

are the postcollision moments. Note that since the equilibrium populations are exact, the equilibrium moments $M^{\mathrm{eq}}$ coincide with the Maxwell-Boltzmann moments.

In the following, we also drop the superscript λ for simplicity. Using the Taylor expansion up to third order one can write

$$M^*(\boldsymbol{x}-\boldsymbol{v}_i\delta t, t-\delta t) = M^*(\boldsymbol{x},t) - \delta t D_i M^* + \frac{\delta t^2}{2} \times \left(D_i^2 M^* - D_i v_{i\alpha}\partial_\alpha M^*\right) + \mathcal{O}(\delta t^3), \tag{29}$$

where $D_i = \partial_t + v_{i\alpha}\partial_\alpha$ is the material derivative. Finally, substituting the expansion Eq. (29) into Eq. (27) results in

$$\begin{aligned}\delta t D_i f_i - \frac{\delta t^2}{2} D_i^2 f_i &= -\omega f_i^{\mathrm{neq}} + \delta t D_i\left(\omega f_i^{\mathrm{neq}}\right) + \delta t D_i \mathcal{M}_i^{-1} M^* \\ &- \frac{\delta t^2}{2} D_i^2\left(\omega f_i^{\mathrm{neq}}\right) - \frac{\delta t^2}{2}\mathcal{M}_i^{-1} D_i v_{i\alpha}\partial_\alpha M^* \\ &- \frac{\delta t^2}{2} D_i\left(D_i \mathcal{M}_i^{-1} M^*\right) - \frac{\delta t^2}{2} D_i \mathcal{M}_i^{-1} D_i M^*. \end{aligned}\tag{30}$$

By applying the operator $D_i$ upon the latter equation and neglecting the higher-order terms $\mathcal{O}(\delta t^3)$, we get

$$\begin{aligned}\frac{\delta t^2}{2} D_i^2 f_i = -\frac{\delta t}{2} D_i\left(\omega f_i^{\mathrm{neq}}\right) + \frac{\delta t^2}{2} D_i^2\left(\omega f_i^{\mathrm{neq}}\right) \\ + \frac{\delta t^2}{2} D_i\left(D_i \mathcal{M}_i^{-1} M^*\right).\end{aligned}\tag{31}$$

Eventually, substituting Eq. (31) from Eq. (30) yields

$$\begin{aligned}D_i f_i = -\frac{\omega}{\delta t} f_i^{\mathrm{neq}} + D_i\left(\frac{\omega}{2} f_i^{\mathrm{neq}}\right) + D_i \mathcal{M}_i^{-1} M^* \\ - \frac{\delta t}{2} D_i \mathcal{M}_i^{-1} D_i M^* - \frac{\delta t}{2}\mathcal{M}_i^{-1} D_i v_{i\alpha}\partial_\alpha M^*.\end{aligned}\tag{32}$$

To start the analysis, first the following expansions are introduced:

$$\begin{aligned} f_i &= f_i^{(0)} + \epsilon f_i^{(1)} + \epsilon^2 f_i^{(2)}, \\ M^* &= M^{*(0)} + \epsilon M^{*(1)} + \epsilon^2 M^{*(2)}, \\ \partial_t &= \epsilon\partial_t^{(1)} + \epsilon^2\partial_t^{(2)}, \\ \partial_\alpha &= \epsilon\partial_\alpha^{(1)}. \end{aligned}\tag{33}$$

Rearranging the equations and collecting the corresponding terms on each order yields

$$\mathcal{O}(\epsilon^0): \; f_i^{(0)} = f_i^{\mathrm{eq}} \;\rightarrow M^{(0)} = M^{\mathrm{eq}}, \tag{34}$$

$$\mathcal{O}(\epsilon^1): D_i^{(1)} f_i^{(0)} - D_i^{(1)}\mathcal{M}_i^{-1} M^{(0)} = -\frac{\omega}{\delta t} f_i^{(1)}, \tag{35}$$

$$\begin{aligned}\mathcal{O}(\epsilon^2): \; \partial_t^{(2)} f_i^{(0)} + D_i^{(1)}\left[\left(1-\frac{\omega}{2}\right) f_i^{(1)}\right] \\ = -\frac{\omega}{\delta t} f_i^{(2)} + \partial_t^{(2)}\mathcal{M}_i^{-1} M^{(0)} + D_i^{(1)}\mathcal{M}_i^{-1}\left(1-\frac{\omega}{2}\right) M^{(1)} \\ - \frac{\delta t}{2}\mathcal{M}_i^{-1} D_i^{(1)}(\mathcal{M} V_\alpha \mathcal{M}^{-1})\partial_\alpha M^{(0)},\end{aligned}\tag{36}$$

where $V_\alpha = \mathrm{diag}(v_\alpha)$. Recalling that $f_i^{(0)} = \mathcal{M}_i^{-1} M^{(0)}$, Eq. (35) is rewritten as

$$\mathcal{M}_i^{-1}\partial_t^{(1)} M^{(0)} + v_{i\alpha}\mathcal{M}_i^{-1}\partial_\alpha^{(1)} M^{(0)} = -\frac{\omega}{\delta t} f_i^{(1)}, \tag{37}$$

where we can derive the first-order evolution equation for the equilibrium moments by multiplying both sides of Eq. (37) by $\mathcal{M}$ and recalling that $M^{(1)} = \mathcal{M} f^{(1)}$:

$$\mathcal{D}^{(1)} M^{(0)} = -\frac{\omega}{\delta t} M^{(1)}, \tag{38}$$

where $\mathcal{D} = \partial_t + \mathcal{M} V_\alpha \mathcal{M}^{-1}\partial_\alpha$. Finally, the second-order kinetic equation (36) can be rearranged to

$$\begin{aligned}\partial_t^{(2)} M^{(0)} + \mathcal{D}^{(1)}\left[\left(1-\frac{\omega}{2}\right) M^{(1)}\right] \\ = -\frac{\omega}{\delta t} M^{(2)} - \frac{\delta t}{2}\mathcal{D}^{(1)}(\mathcal{M} V_\alpha \mathcal{M}^{-1})\partial_\alpha M^{(0)},\end{aligned}\tag{39}$$

where $M^{(2)} = \mathcal{M} f^{(2)}$.

### C. Conservation equations

With the split kinetic equations at three different orders, we are now able to derive the hydrodynamic limit of the present kinetic model. However, due to the dependence of the multiscale kinetic equations on the linear mapping matrix $\mathcal{M}$ and its corresponding inversion, we specify a lattice to proceed with the analysis. In the following, we consider the most commonly used lattices in one- and two-dimensional applications, i.e., $D1Q3$, $D1Q5$, $D2Q9$, and $D2Q25$, where the peculiar velocities $\boldsymbol{c}_i$ and the lattice reference temperature $T_{\mathrm{L}}$ in Eq. (2) are known for each of them [18].

#### *1. D1Q3*

The three linearly independent moments in Eq. (18) are

$$\begin{aligned} M_{00} &= \sum_i f_i, \\ M_{10} &= \sum_i f_i v_i, \\ M_{20} &= \sum_i f_i v_i^2, \end{aligned}\tag{40}$$

which all are conserved moments and coincide with their counterpart equilibrium ones. Hence, the mass, momentum, and total energy conservation implies that $M^{(1)} = M^{(2)} = [0,0,0]^\dagger$. The inversion of the mapping matrix is obtained as

$$\mathcal{M}^{-1} = \begin{bmatrix} 1-\frac{u^2}{\theta} & \frac{2u}{\theta} & \frac{-1}{\theta} \\ \frac{u^2-\sqrt{\theta}u}{2\theta} & \frac{\sqrt{\theta}-2u}{2\theta} & \frac{1}{2\theta} \\ \frac{u^2+\sqrt{\theta}u}{2\theta} & \frac{-\sqrt{\theta}-2u}{2\theta} & \frac{1}{2\theta} \end{bmatrix}, \tag{41}$$

where it is observed that

$$\sum_i \mathcal{M}_{ij}^{-1} = \begin{cases} 1, & j=1 \\ 0 & \text{otherwise.} \end{cases} \tag{42}$$

Finally, the first-order equations are recovered from Eq. (38) as

$$\partial_t^{(1)}\begin{bmatrix}\rho \\ \rho u \\ \rho u^2 + \rho\theta T_{\mathrm{L}}\end{bmatrix} + \partial_\alpha^{(1)}\begin{bmatrix}\rho u \\ \rho u^2 + \rho\theta T_{\mathrm{L}} \\ 2\rho u H\end{bmatrix} = \begin{bmatrix}0\\0\\0\end{bmatrix}, \tag{43}$$

where $H = \theta/2 + u^2/2$ is the total enthalpy and $h = \theta/2$ is the specific enthalpy, which implies $C_p = 3/2$ for an ideal

gas. Similarly, the second-order equations are obtained from Eq. (39):

$$\partial_t^{(2)}\begin{bmatrix}\rho\\ \rho u\\ \rho u^2+\rho\theta T_{\mathrm{L}}\end{bmatrix}=-\frac{\delta t}{2}\begin{bmatrix}0\\ X_M^{(1),(1)}\\ X_E^{(1),(1)}\end{bmatrix}, \tag{44}$$

where

$$X_M^{(1),(1)}=\rho\partial_\alpha^{(1)}u\partial_\alpha^{(1)}\theta, \tag{45}$$

$$X_E^{(1),(1)}=\rho\partial_t^{(1)}\theta\partial_\alpha^{(1)}u+\rho\partial_\alpha^{(1)}\theta\left(\partial_t^{(1)}u+3\partial_\alpha^{(1)}u^2\right), \tag{46}$$

and the double superscript denotes the product of two first-order terms. Finally, the hydrodynamic equations are recovered by collecting the first- and second-order equations Eqs. (43) and (44) and recalling the expansions Eq. (33),

$$\partial_t\begin{bmatrix}\rho\\ \rho u\\ \rho u^2+\rho\theta T_{\mathrm{L}}\end{bmatrix}+\partial_\alpha\begin{bmatrix}\rho u\\ \rho u^2+\rho\theta T_{\mathrm{L}}\\ 2\rho uH\end{bmatrix}=\begin{bmatrix}0\\ -X_M\\ -X_E\end{bmatrix}, \tag{47}$$

where

$$X_M=\delta t\rho\partial_\alpha u\partial_\alpha\theta, \tag{48}$$

$$X_E=\frac{\delta t}{2}(\partial_\alpha(\rho\theta)\partial_\alpha u^2-\partial_\alpha\theta\partial_\alpha(\rho\theta T_{\mathrm{L}})), \tag{49}$$

are the error terms in the momentum and energy equations, respectively. As a conclusion, the thermohydrodynamic equations for the $D1Q3$ lattice are recovered as the one-dimensional compressible Euler equations (vanishing viscosity) with error terms of $\mathcal{O}(\delta t)$ in the momentum and energy equations.

### 2. D1Q5

In this section, we consider the $D1Q5$ lattice with the discrete velocities $\boldsymbol{C}=\{0,\pm m,\pm n\}$, where $m=rn$ and $r=(\sqrt{5}-\sqrt{2})/\sqrt{3}$ is the ratio of the roots of the fifth-order Hermite polynomial [18]. The weights and the lattice reference temperature are defined as

$$w_0=\frac{-3r^4-3+54r^2}{75r^2}, \tag{50}$$

$$w_{\pm m}=\frac{9r^4-6-27r^2}{300r^2(r^2-1)}, \tag{51}$$

$$w_{\pm n}=\frac{9-6r^4-27r^2}{300(1-r^2)}, \tag{52}$$

$$T_{\mathrm{L}}=\frac{m^2(r^2+1)}{10r^2}, \tag{53}$$

where we choose $m=1$. The independent system of moments is $M=[M_{00},M_{10},M_{20},M_{30},M_{40}]^\dagger$ with the nonequilibrium moments

$$M^{(k)}=\left[0,0,0,\sum f_i^{(k)}v_i^3,\sum f_i^{(k)}v_i^4\right]^\dagger,\quad k=1,2. \tag{54}$$

Once again, we observe that relation Eq. (42) holds for this lattice structure as well. According to Eq. (38), the first-order equations are derived correctly as in Eq. (43). On the other hand, Eq. (39) gives the second-order equations as

$$\partial_t^{(2)}\begin{bmatrix}\rho\\ \rho u\\ \rho u^2+\rho\theta T_{\mathrm{L}}\end{bmatrix}+\partial_\alpha^{(1)}\begin{bmatrix}0\\ 0\\ (1-\omega/2)q^{(1)}\end{bmatrix}=\begin{bmatrix}0\\ 0\\ 0\end{bmatrix}, \tag{55}$$

where

$$q^{(1)}=\sum_i f_i^{(1)}v_i^3=-\frac{\delta t}{\omega}\left(\partial_t^{(1)}Q^{\mathrm{eq}}+\partial_\alpha^{(1)}R^{\mathrm{eq}}\right) \tag{56}$$

is the nonequilibrium heat flux derived from Eq. (38) and

$$Q^{\mathrm{eq}}=\sum_i\rho w_i v_i^3, \tag{57}$$

$$R^{\mathrm{eq}}=\sum_i\rho w_i v_i^4, \tag{58}$$

are the equilibrium high-order moments coinciding with their Maxwell-Boltzmann expressions. It is straightforward to show

$$q^{(1)}=-\frac{2\delta t}{\omega}\left((3-\gamma)pu\partial_\alpha^{(1)}u+pC_p\partial_\alpha^{(1)}T\right). \tag{59}$$

Since using a single population leads to a fixed specific heat $\gamma=(D+2)/D$, the viscous part in Eq. (59) vanishes, while the Fourier heat flux is retained. This is in contrast to the $D1Q3$ lattice, where, due to the same number of velocities and conservation laws, the Fourier heat flux in the energy equation vanishes as well as the viscous terms in the momentum and energy equations. Finally, the thermohydrodynamic equations recovered by using the $D1Q5$ lattice are obtained as

$$\partial_t\begin{bmatrix}\rho\\ \rho u\\ \rho u^2+\rho\theta T_{\mathrm{L}}\end{bmatrix}+\partial_\alpha\begin{bmatrix}\rho u\\ \rho u^2+\rho\theta T_{\mathrm{L}}\\ 2\rho uH\end{bmatrix}=\begin{bmatrix}0\\ 0\\ 2\partial_\alpha(k\partial_\alpha T)\end{bmatrix}, \tag{60}$$

where $k=(1/\omega-1/2)p\delta tC_p$ is the conductivity and $C_p=3/2$.

The most distinctive feature of the recovered equations is the absence of error terms in the momentum and energy equations. Although the Galilean invariance of $D1Q5$ models has been verified in isothermal setups [18], here we observe a somewhat different behavior. The adaptive construction of discrete velocities in PonD guarantees Galilean invariance even with the $D1Q3$ lattice. Having the exact equilibrium, all the recovered equilibrium moments up to fourth order [Eq. (58))] match with their Maxwell-Boltzmann counterparts. However, we observe that the insufficiency of the mapping matrix $\mathcal{M}$ and its inversion in the $D1Q3$ lattice is responsible for the generated errors [see Eq. (36)]. According to the invariant-moment rule Eq. (19), the sufficiency of linearly independent moments is crucial for a meaningful transformation between two reference frames. Not having met this criterion, the $D1Q3$ (and its two-dimensional tensor product as we will see later) is unable to provide an error-free transformation. On the other hand, due to its sufficient system of moments, the $D1Q5$ lattice does not introduce errors during the transformation and, together with the fully recovered equilibrium moments, the hydrodynamic equations are derived in their correct form.

### 3. D2Q9

The $D2Q9$ lattice can be considered as the tensor product of two $D1Q3$ lattices. The independent moment system in this type of lattice structure is

$$M = [M_{00}, M_{10}, M_{01}, M_{11}, M_{20}, M_{02}, M_{21}, M_{12}, M_{22}]^{\dagger}, \quad (61)$$

where the nonequilibrium moments are

$$M^{(k)} = \left[0, 0, 0, M_{11}^{(k)}, M_{20}^{(k)}, M_{02}^{(k)}, M_{21}^{(k)}, M_{12}^{(k)}, M_{22}^{(k)}\right]^{\dagger}, \quad (62)$$

and the conservation of energy implies $M_{20}^{(k)} + M_{02}^{(k)} = 0$.

The first-order equations are derived as

$$\partial_t^{(1)} \begin{bmatrix} \rho \\ \rho u_\alpha \\ P_{\alpha\alpha}^{\rm eq} \end{bmatrix} + \partial_\beta^{(1)} \begin{bmatrix} \rho u_\beta \\ P_{\alpha\beta}^{\rm eq} \\ 2\rho u_\beta H \end{bmatrix} = \begin{bmatrix} 0 \\ 0 \\ 0 \end{bmatrix}, \quad (63)$$

where

$$P_{\alpha\beta}^{\rm eq} = \rho u_\alpha u_\beta + \rho\theta T_{\rm L}\delta_{\alpha\beta} \quad (64)$$

is the equilibrium pressure tensor. The second-order equations are obtained as

$$\partial_t^{(2)} \begin{bmatrix} \rho \\ \rho u_\alpha \\ P_{\alpha\alpha}^{\rm eq} \end{bmatrix} + \partial_\beta^{(1)} \begin{bmatrix} 0 \\ (1-\omega/2)P_{\alpha\beta}^{(1)} \\ (1-\omega/2)Q_{\alpha\alpha\beta}^{(1)} \end{bmatrix} = \begin{bmatrix} 0 \\ \mathcal{O}(\delta t) \\ \mathcal{O}(\delta t) + 3q \end{bmatrix}, \quad (65)$$

where $P_{\alpha\beta}^{(1)}$ is the nonequilibrium pressure tensor derived from Eq. (38),

$$P_{\alpha\beta}^{(1)} = -\left(\frac{\delta t}{\omega}\right)\left(\partial_t^{(1)} P_{\alpha\beta}^{\rm eq} + \partial_\gamma^{(1)} Q_{\alpha\beta\gamma}^{\rm eq}\right), \quad (66)$$

and

$$Q_{\alpha\beta\gamma}^{\rm eq} = \rho u_\alpha u_\beta u_\gamma + \rho\theta T_{\rm L}(u_\alpha\delta_{\beta\gamma} + u_\beta\delta_{\alpha\gamma} + u_\gamma\delta_{\alpha\beta}). \quad (67)$$

Using the first-order Eq. (63), it can be shown that

$$\begin{aligned} &\partial_t^{(1)} P_{\alpha\beta}^{\rm eq} + \partial_\gamma^{(1)} Q_{\alpha\beta\gamma}^{\rm eq} \\ &\quad = p\left(\partial_\alpha^{(1)} u_\beta + \partial_\beta^{(1)} u_\alpha\right) + \left(p - \rho c_s^2\right)\partial_\gamma^{(1)} u_\gamma \delta_{\alpha\beta}, \end{aligned} \quad (68)$$

where $c_s^2 = \gamma T$ is the speed of sound of an ideal gas.

The second-order equation for the energy part Eq. (65) is originally derived as

$$\begin{aligned} &\partial_t^{(2)}\left(P_{xx}^{\rm eq} + P_{yy}^{\rm eq}\right) + \partial_x^{(1)}\left[\left(1-\frac{\omega}{2}\right)Q_{xyy}^{(1)}\right] \\ &\quad + \partial_y^{(1)}\left[\left(1-\frac{\omega}{2}\right)Q_{xxy}^{(1)}\right] + 3u\partial_x^{(1)}\left[\left(1-\frac{\omega}{2}\right)P_{xx}^{(1)}\right] \\ &\quad + 3v\partial_y^{(1)}\left[\left(1-\frac{\omega}{2}\right)P_{yy}^{(1)}\right] = \mathcal{O}(\delta t), \end{aligned} \quad (69)$$

while the closure relation

$$Q_{nnn}^{(1)} = 3u_n P_{nn}^{(1)}, \ n = x, y, \quad (70)$$

has been used to render the final equation in a concise form. As a result, the error term $3q$ appears in the right-hand side (RHS) of the energy equation, where

$$q = \left(1-\frac{\omega}{2}\right)\left[P_{xx}^{(1)}\partial_x^{(1)} u + P_{yy}^{(1)}\partial_y^{(1)} v\right]. \quad (71)$$

However, the nonequilibrium heat flux $Q_{\alpha\alpha\beta}^{(1)}$ is computed in two separate steps. While the terms $Q_{xxy}^{(1)}$ and $Q_{xyy}^{(1)}$ are included in the nonequilibrium system of moments in Eq. (38), the diagonal elements $Q_{xxx}^{(1)}$ and $Q_{yyy}^{(1)}$ are slaved by the closure Eq. (70). Consequently, the final form of the nonequilibrium heat flux is derived as

$$Q_{\alpha\alpha\beta}^{(1)} = -\frac{\delta t}{\omega}\left[\partial_t^{(1)} Q_{\alpha\alpha\beta}^{\rm eq} + \partial_\alpha^{(1)} R_{\alpha\beta}^{\rm eq} - 3\rho\theta T_{\rm L}\partial_\beta^{(1)}(\theta T_{\rm L})\right], \quad (72)$$

where

$$R_{\alpha\beta}^{\rm eq} = 2\rho u_\alpha u_\beta (H + \theta T_{\rm L}) + 2\rho\theta T_{\rm L} H\delta_{\alpha\beta} \quad (73)$$

is the fourth-order equilibrium moment and from Eq. (63) one can compute

$$\begin{aligned} \partial_t^{(1)} Q_{\alpha\alpha\beta}^{\rm eq} + \partial_\alpha^{(1)} R_{\alpha\beta}^{\rm eq} &= 2pu_\alpha\left(\partial_\alpha^{(1)} u_\beta + \partial_\beta^{(1)} u_\alpha\right) \\ &\quad + 2\left(p - \rho c_s^2\right)\partial_\gamma^{(1)} u_\gamma u_\beta + 2p\partial_\beta^{(1)} h, \end{aligned} \quad (74)$$

where $h = (D/2+1)\theta T_{\rm L}$. On an interesting note, we observe that the insufficiency of the diagonal elements of the third-order nonequilibrium moment has caused an anomaly in the appearance of the nonequilibrium heat flux Eq. (72). The nonconventional term in the RHS of Eq. (72) will contribute to the Fourier heat flux and will alter the value of the Prandtl number as we will see later. On a separate comment, we note that, similar to the $D1Q3$ case, there exist error terms with the order of $\mathcal{O}(\delta t)$ in the momentum and energy equations.

Finally, the hydrodynamic equations for the $D2Q9$ lattice are recovered as

$$\partial_t \begin{bmatrix} \rho \\ \rho u_\alpha \\ \rho E \end{bmatrix} + \partial_\beta \begin{bmatrix} \rho u_\beta \\ \rho u_\alpha u_\beta + p\delta_{\alpha\beta} + \tau_{\alpha\beta} \\ \rho u_\beta H + u_\alpha \tau_{\alpha\beta} + q_\beta \end{bmatrix} = \begin{bmatrix} 0 \\ \mathcal{O}(\delta t) \\ \mathcal{O}(\delta t) + 3q \end{bmatrix}, \quad (75)$$

where

$$\tau_{\alpha\beta} = -\mu\left(\partial_\alpha u_\beta + \partial_\beta u_\alpha - \frac{2}{D}\partial_\gamma u_\gamma \delta_{\alpha\beta}\right) - \eta\partial_\gamma u_\gamma \delta_{\alpha\beta} \quad (76)$$

is the shear stress tensor and $q_\beta = -k\partial_\beta T$ is the Fourier heat flux. The shear viscosity, bulk viscosity, and the conductivity are

$$\mu = \left(\frac{1}{\omega} - \frac{1}{2}\right)p\delta t, \quad (77)$$

$$\eta = \left(\frac{1}{\omega} - \frac{1}{2}\right)\left(\frac{D+2}{D} - \gamma\right)p\delta t, \quad (78)$$

$$k = \left(\frac{1}{\omega} - \frac{1}{2}\right)\left(\frac{D-1}{2}\right)p\delta t, \quad (79)$$

respectively. We note that the bulk viscosity vanishes at the limit of a monatomic ideal gas, as expected [21].

The error terms in the momentum and energy equations are found as

$$X_{\alpha M} = -\delta t\,\rho U_{\alpha\beta}\partial_\beta\theta, \quad (80)$$

$$\begin{aligned} X_E = &-\frac{\delta t}{2}\left(-\rho\frac{\theta}{C_v}(\partial_\alpha u_\alpha)^2 - \partial_\alpha\theta\partial_\alpha(\rho\theta T_{\rm L}) + 4\rho u_\alpha\partial_\beta\theta U_{\beta\alpha}\right) \\ &- 3\bar{q}, \end{aligned} \quad (81)$$

where

$$\boldsymbol{U} = \nabla \boldsymbol{u} \odot \boldsymbol{I} = \begin{bmatrix} \partial_x u & 0 \\ 0 & \partial_y v \end{bmatrix} \tag{82}$$

is the Hadamard product of the velocity gradient tensor and the identity matrix and

$$\bar{q} = \mu[(3-\gamma)((\partial_x u)^2 + (\partial_y v)^2) + 2(1-\gamma)\partial_x u \partial_y v]. \tag{83}$$

Finally, the Prandtl number is found as

$$\mathrm{Pr} = \frac{\mu C_p}{k} = \frac{D+2}{D-1}, \tag{84}$$

which amounts to 4 in two dimensions as reported in [19].

#### *4. D2Q25*

The $D2Q25$ lattice is a tensor product of two $D1Q5$ lattices with the independent moment system of

$$M_{mn} = \sum_i f_i v_{ix}^m v_{iy}^n, \begin{matrix} m = 0, \ldots, 4 \\ n = 0, \ldots, 4, \end{matrix} \tag{85}$$

where the property Eq. (42) holds for the inversion mapping matrix $\mathcal{M}^{-1}$. While the first-order equations coincide with those obtained in Eqs. (63), the second-order equations are derived as

$$\partial_t^{(2)} \begin{bmatrix} \rho \\ \rho u_\alpha \\ P_{\alpha\alpha}^{\mathrm{eq}} \end{bmatrix} + \partial_\beta^{(1)} \begin{bmatrix} 0 \\ (1-\omega/2)P_{\alpha\beta}^{(1)} \\ (1-\omega/2)Q_{\alpha\alpha\beta}^{(1)} \end{bmatrix} = \begin{bmatrix} 0 \\ 0 \\ 0 \end{bmatrix}. \tag{86}$$

The nonequilibrium pressure tensor is recovered as in Eq. (66); however, the nonequilibrium heat flux is derived as

$$Q_{\alpha\alpha\beta}^{(1)} = -\frac{\delta t}{\omega}\left[\partial_t^{(1)} Q_{\alpha\alpha\beta}^{\mathrm{eq}} + \partial_\alpha^{(1)} R_{\alpha\beta}^{\mathrm{eq}}\right]. \tag{87}$$

Finally, the hydrodynamic equations for the $D2Q25$ lattice are recovered as

$$\partial_t \begin{bmatrix} \rho \\ \rho u_\alpha \\ \rho E \end{bmatrix} + \partial_\beta \begin{bmatrix} \rho u_\beta \\ \rho u_\alpha u_\beta + p\delta_{\alpha\beta} + \tau_{\alpha\beta} \\ \rho u_\beta H + u_\alpha \tau_{\alpha\beta} + q_\beta \end{bmatrix} = \begin{bmatrix} 0 \\ 0 \\ 0 \end{bmatrix}, \tag{88}$$

where the shear stress tensor $\tau_{\alpha\beta}$ is defined in Eq. (76) with the dynamic viscosity Eq. (77). The conductivity, however, is recovered as

$$k = \left(\frac{1}{\omega} - \frac{1}{2}\right) p\delta t \left(\frac{D+2}{2}\right), \tag{89}$$

which implies $\mathrm{Pr} = 1$.

Similar to the $D1Q5$ lattice, the hydrodynamic equations are recovered free of error terms.

### D. Variable specific heat

To achieve an arbitrary specific heat $\gamma$, it is conventional to adopt a second population. However, one can assign the second population to either carry the total energy or the extra internal energy. We introduce the following equilibrium for the second population:

$$g_i^{\mathrm{eq}} = 2 f_i^{\mathrm{eq}} \left[\left(C_v - \frac{D}{2}\right)T + (1-\phi)\frac{v_i^2}{2}\right], \tag{90}$$

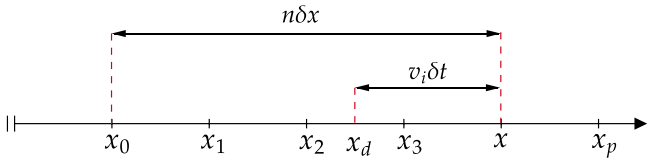


FIG. 2. Schematic of the interpolation process and the collocation points during the semi-Lagrangian advection.

where $\phi = 1$ implies that the excess internal energy as the difference from a $D$-dimensional gas is conserved by the $g$ population, while the kinetic energy is maintained by the $f$ population [17]. On the other hand, $\phi = 0$ corresponds to the conservation of the total energy by the $g$ population. Consequently, the total energy is computed as

$$2\rho E = 2\rho e + \rho u^2 = \sum_i g_i + \phi \sum_i f_i v_i^2. \tag{91}$$

Since the hydrodynamic equations for the $D2Q25$ lattice are free of error terms, it seems natural to choose $\phi = 1$ so the equilibrium function of the second population is only a function of temperature and free of velocity terms. However, the choice of $\phi = 1$ for the $D2Q9$ lattice will retain the error terms in the momentum and total energy equations, with the only difference that the specific heat will possess an arbitrary value instead of that of a monatomic ideal gas. In this case, the Prandtl number becomes

$$\mathrm{Pr} = \frac{2\gamma}{3-\gamma}, \tag{92}$$

which limits the value of the adiabatic exponent to $\gamma = 3$ as higher values will amount to unphysical answers. On the other hand, choosing $\phi = 0$ will remove the errors from the total energy equation. Since there will be no closure relation for the diagonal elements of the nonequilibrium third-order moment, the Prandtl number will take its natural value $\mathrm{Pr} = 1$, independent of the choice of $\gamma$. Nevertheless, a variable Prandtl number can always be achieved by using two relaxation parameters [17].

### E. Interpolation

So far, the analysis has been carried out assuming a continuous space, whereas one must account for the interpolation of transformed populations during the advection process. As mentioned before, the departure point accessed during the semi-Lagrangian advection does not essentially coincide with a grid point and a set of collocation points is required to interpolate for the missing information.

In order to proceed with the analysis, we consider the discretized form Eq. (17), where $N$ number of points are used for the interpolation. Without loss of generality, we assume $v_i > 0$. The departure point will be located on an off-grid point $x_d = x - v_i\delta t$, where $x$ is a grid point. Depending on the order of the interpolation, a set of grid points $x_p$ around the departure point will be used for the interpolation process. We assume that the first point of this stencil is located in the distance $n\delta x$ from the monitoring point $x$ such that $x_0 = x - n\delta x$, where $n$ is an integer (see Fig. 2). The advection Eq. (17) is

recast in the following form:

$$f_i^{\lambda}(x,t) = \sum_{p=0}^{N-1} l_p \mathcal{M}_{i,\lambda}^{-1} M^*(x_p, t-\delta t), \tag{93}$$

where $l_p$ are the interpolation weights. At this point, no explicit type of the interpolation function is assumed and the weights $l_p$ or their properties remain to be derived. Considering that $x_p = x-(n-p)\delta x$, one can expand Eq. (93) using the Taylor series up to third-order terms,

$$\begin{aligned} f_i(x,t) &= \sum_p l_p \mathcal{M}_i^{-1} \\ &\times \left( M^*(x,t) - \delta t \bar{D}_p M^*(x,t) + \frac{\delta t^2}{2} \bar{D}_p^2 M^*(x,t) \right) \\ &= f_i^*(x,t) \sum_p l_p - \delta t \mathcal{M}_i^{-1} \sum_p l_p \bar{D}_p M^*(x,t) \\ &+ \frac{\delta t^2}{2} \mathcal{M}_i^{-1} \sum_p l_p \bar{D}_p^2 M^*(x,t), \end{aligned} \tag{94}$$

where $\bar{D}_p = \partial_t + (n-p)(\delta x/\delta t)\partial_x$, $p = 0 : N-1$.

In the following, we compute the individual terms in Eq. (94). In order to be consistent, any interpolation scheme requires the weights to sum to unity, i.e.,

$$\sum_p l_p = 1. \tag{95}$$

The other terms are computed as follows:

$$\sum_p l_p \bar{D}_p M^* = \bar{D}_0 M^* - \sum_p l_p p \frac{\delta x}{\delta t} \partial_x M^*, \tag{96}$$

$$\begin{aligned} \sum_p l_p \bar{D}_p^2 M^* &= \bar{D}_0^2 M^* + \left( \sum_p l_p p^2 - 2n \sum_p l_p p \right) \\ &\times \frac{\delta x^2}{\delta t^2} \partial_{xx} M^* - 2 \sum_p l_p p \frac{\delta x}{\delta t} \partial_{xt} M^*. \end{aligned} \tag{97}$$

In a moment-conserving interpolation function [22,23], we have the property

$$\sum_p l_p (p\delta x)^r = (x_d - x_0)^r, \tag{98}$$

where the number of conserved moments $r$ depends on the order of the interpolation function. Hence, we require the interpolation scheme to obey the property Eq. (98) with $r = 2$ at least. This implies that a stencil with a minimum of three points must be used for the interpolation.

Substituting Eq. (98) in Eqs. (96) and (97) leads to

$$\sum_p l_p \bar{D}_p M^* = \partial_t M^* + v_i \partial_x M^* = D_i M^*, \tag{99}$$

$$\begin{aligned} \sum_p l_p \bar{D}_p^2 M^* &= \partial_{tt} M^* + 2 v_i \partial_{xt} M^* + v_i^2 \partial_{xx} M^* \\ &= D_i^2 M^* - D_i v_i \partial_x M^*. \end{aligned} \tag{100}$$

It can be simply verified that once the averaged terms Eqs. (99) and (100) are plugged into Eq. (94), the kinetic equation of the continuous case Eq. (30) is recovered. Therefore, all the analyses presented so far are also valid when the interpolation procedure is included provided that the interpolation function encompasses three support points at least and abides the moment-conserving property.

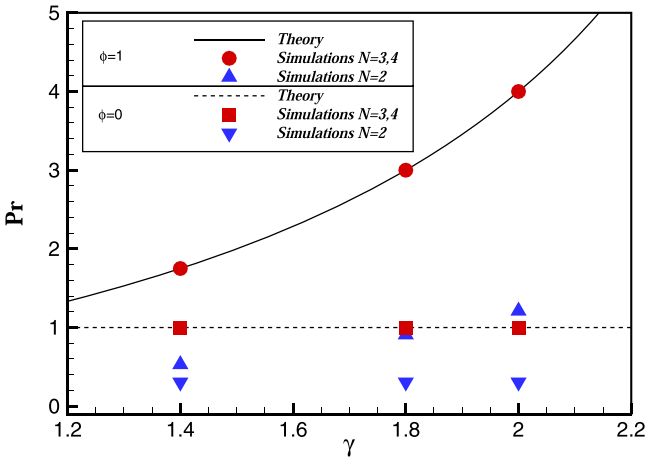


FIG. 3. The measured Prandtl number against the adiabatic exponent using the $D2Q9$ lattice and different values of $\phi$.

### F. Prandtl number

In Sec. III D, it was shown that the choice of equilibrium for the second population for a standard lattice such as $D2Q9$ will affect the recovered energy equation. Besides the unwanted error terms, the Prandtl number obtained by the Chapman-Enskog analysis will be a rational function of the specific heat, i.e., Eq. (92), if only the extra internal energy is assigned to the second population ($\phi = 1$). On the other hand, choosing $\phi = 0$ will remove the error terms and recover $\mathrm{Pr} = 1$. Moreover, we illustrated that in order to have a consistent scheme, the interpolation function must feature a moment-conserving property with at least three support points.

To verify our analysis, we conduct the standard test case to measure the value of the Prandtl number [19]. We choose the $D2Q9$ lattice with the first-order ($N = 2, r = 1$), second-order ($N = 3, r = 2$), and third-order ($N = 4, r = 3$) Lagrange interpolation schemes. Figure 3 shows that our analyses are consistent with the simulations. It is also clearly visible that the interpolation scheme with $r < 2$ deviates from the underlying theoretical values.

### G. Convergence study

The standard LBM is a second-order accurate scheme in space and time featuring $\delta x = \delta t = 1$. On the other hand, it is well known that the compressibility errors in the standard LBM scale with $\mathrm{Ma}^2$ and the Navier-Stokes equations (NSE) is recovered with error terms proportional to $\mathrm{Kn}^2$, where Kn is the Knudsen number [2]. However, it has been shown that the semi-Lagrangian LBM (SLLBM) [12,24] can achieve higher orders by decoupling the time step from the grid spacing provided that the time step - in another sense the CFL (Courant-Friedrichs-Lewy) number - and the Mach number are kept relatively low. Then, high-order interpolation

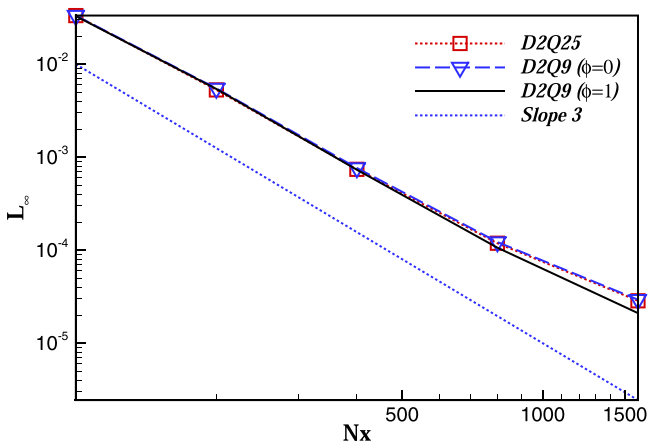


FIG. 4. Convergence of the $L_\infty$ error in the linear advection test: all schemes recover the underlying order of accuracy.

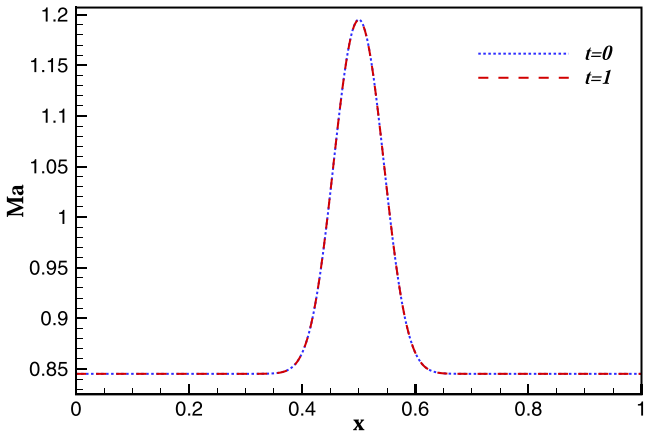


FIG. 5. Mach profile of the linear advection test at $\delta t = 10^{-4}$, using the $D2Q9$ lattice, $Nx = 400$, and $\phi = 0$.

functions can lead to a high spatial order of accuracy. In this case, as shown and discussed in [12,25], the discretization errors are on the order of $\mathcal{O}(\min(\delta x^N/\delta t, \delta x^{N-1}))$. On the other hand, we have shown that using nine discrete velocities in the PonD framework will introduce error terms on the order of $\mathcal{O}(\delta t)$ in the momentum and energy equations. Finally, one can summarize that the present model includes error terms as deviations from the full compressible NSE, which are on the order of

$$D1Q3, D2Q9 : \mathcal{O}\left(\min\left(\frac{\delta x^N}{\delta t}, \delta x^{N-1}\right), \delta t, \mathrm{Kn}^2\right),$$
$$D1Q5, D2Q25 : \mathcal{O}\left(\min\left(\frac{\delta x^N}{\delta t}, \delta x^{N-1}\right), \delta t^2, \mathrm{Kn}^2\right), \quad (101)$$

where the compressibility error $\mathcal{O}(\mathrm{Ma}^2)$ is eliminated thanks to the exact equilibrium function. In the following, we will assess the validity of these results by conducting numerical simulations. To verify the spatial discretization errors, a density profile is advected with the following initial conditions:

$$\rho_0(x) = 1 + \exp(-300(x-0.5)^2), \ 0 \leqslant x \leqslant 1,$$
$$p_0(x) = 1,$$
$$u_0(x) = 1. \quad (102)$$

While the number of grid points $Nx$ is varied in this simulation, the time step is fixed at a small value $\delta t = 10^{-4}$ to eliminate the chance of dominance of temporal errors. A third-order Lagrange interpolation function with four support points is adopted in this simulation and the value of the specific heat is chosen as $\gamma = 1.4$. We let the simulations run until $t = 1$, which corresponds to one period in time. To reflect the maximum error throughout the domain, the $L_\infty$ error defined as

$$L_\infty = \max\left(\left|\frac{\rho(x) - \rho_0(x)}{\rho_0(x)}\right|\right) \quad (103)$$

is measured to investigate the error convergence.

Figure 4 shows that the underlying order of accuracy of the interpolation function is recovered for both $D2Q25$ and $D2Q9$ lattices and is independent of the choice of the equilibrium function for the second population, as expected. Figure 5 shows the local Mach number for number of grid points $N = 400$. It is noticed that the range of the Mach number in this simulation is significantly high, whereas it was shown that the compressibility errors in SLLBM [24] can already prevail at $\mathrm{Ma} = 0.1$. This is due to the Galilean-invariant nature of the PonD model where it eliminates the compressibility errors by designing particles at the comoving reference frame and the exact collision seen from those particles.

To study the behavior of the temporal errors, we simulate the advection of a vortex by a uniform flow at $\mathrm{Ma}_a = U_a/\sqrt{\gamma T_0} = 0.845$ [16]. The velocity field in the cylindrical coordinates and in the advected reference frame is $u_\theta(r) = u_{\max} r \exp[(1-r^2)/2]$, where $r = r'/R$ is the reduced radius and $R$ is the radius of the vortex. The vortex Mach number is defined based on the maximum tangential velocity in the comoving reference frame, $\mathrm{Ma}_v = u_{\max}/\sqrt{\gamma T_0}$, and is fixed to $\mathrm{Ma} = 0.4$. The Reynolds number is fixed to $\mathrm{Re} = 2U_a R/\nu = 6 \times 10^5$ and a $400 \times 400$ grid is used. The vortex is allowed to complete one cycle of rotation during one period of advection and then the $x$ velocity component is measured along the centerline, where its deviation from the exact solution is indicative of errors. This simulation is repeated with different time steps with a fixed advection velocity.

Figure 6 shows the $L_\infty$ errors for both the $D2Q25$ and $D2Q9$ lattices. We see the results are recovered consistently with Eq. (101), where the $D2Q25$ lattice shows second-order convergence, while the $D2Q9$ lattice is first order in time when the excess internal energy is assigned to the $g$ population, i.e., $\phi = 1$. Another interesting point, which rises in this simulation is the nonmonotonic behavior of the temporal errors in the $D2Q25$ lattice. This is due to the competing effect between the $\mathcal{O}(\delta x^N/\delta t)$ and $\mathcal{O}(\delta t^2)$ error terms, when the resolution $\delta x$ and the order of the interpolation $N$ are fixed. Depending on their orders of magnitude, the latter might take over at small time steps and increase the errors as time is refined. At first, a second-order convergence is observed until $U_a \delta t/\delta x = 0.5$. After this point, further refinement results in increasing the errors, implying that the $\mathcal{O}(\delta x^N/\delta t)$ term has become dominant. This reverse effect, which was also reported in [25], is not observed in the $D2Q9$ lattice in this setup since the $\mathcal{O}(\delta t)$

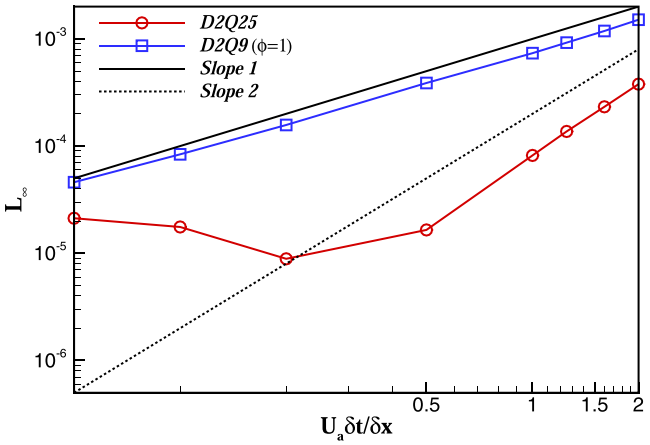


FIG. 6. Time refinement study in the simulation of the advected vortex: convergence of the $L_\infty$ error by decreasing the time step. $400 \times 400$ grid points are used.

terms retain greater magnitude throughout the refinement procedure.

As said earlier, the choice of $\phi$ can affect the recovered energy equation when the $D2Q9$ lattice is used, such that $\phi = 0$ can remove the errors from the energy equation. However, the momentum equation will still have the $\mathcal{O}(\delta t)$ errors and the scheme will be effectively first order in time. To verify this, we augment the postcollision $f$ populations by a forcing term as

$$f_i^*(\boldsymbol{x}, t) = f_i(\boldsymbol{x}, t) + \omega(\rho w_i - f_i)_{(\boldsymbol{x},t)} + \hat{f}_i \delta t, \tag{104}$$

where $\hat{f}_i = \mathcal{M}_i^{-1} \boldsymbol{X}$ and

$$\boldsymbol{X} = [0, X_{xM}, X_{yM}, 0, 0, 0, 0, 0, 0]^\dagger \tag{105}$$

includes the error terms in the momentum equation recovered in Eq. (81). Choosing $\phi = 0$ and forcing out the error terms $X_{\alpha M}$, we repeat the same simulation using the $D2Q9$ lattice. As demonstrated in Fig. 7, the scheme becomes second-order

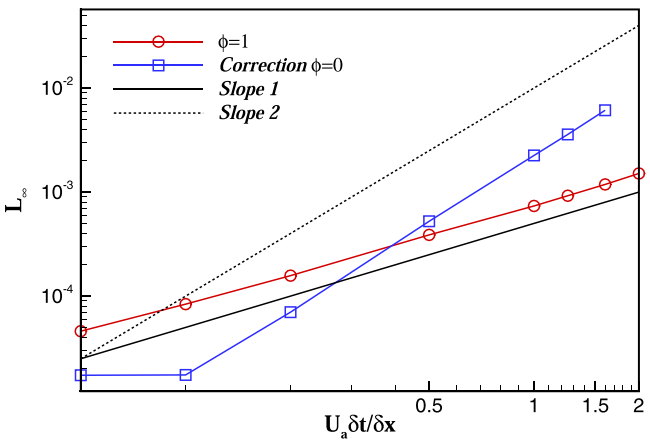


FIG. 7. Time refinement study in the simulation of the advected vortex: convergence of the $L_\infty$ error by decreasing the time step. The $D2Q9$ lattice is used with $\phi = 1$ and $\phi = 0$ augmented by the correction term.

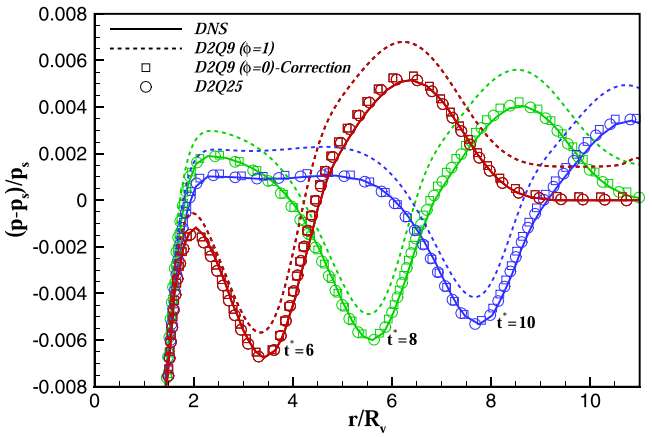


FIG. 8. Radial sound pressure measured at $\theta = -45^\circ$ with respect to the $x$ axis at nondimensional times $t^* = \{6, 8, 10\}$. The governing parameters are $\mathrm{Ma}_a = 1.2$, $\mathrm{Ma}_v = 0.25$, $\mathrm{Re} = 800$, and $\mathrm{Pr} = 0.75$. DNS from [26].

accurate in time once the error terms are corrected. This indicates that the analyses are consistent with simulations.

## IV. BENCHMARK

In this section, the interaction of a vortex with a standing shock front is considered. The Mach number of the vortex is $\mathrm{Ma}_v = 0.25$ and its radius is denoted by $R_v$. When passing through the shock front with the intensity $\mathrm{Ma}_a = 1.2$, sound waves are generated by the vortex. To assess the numerical accuracy of a model, one can measure the sound pressure and compare to the direct numerical simulation (DNS) solution [26]. In this simulation, the Reynolds number is defined as $\mathrm{Re} = a_\infty R_v/\nu$, where $a_\infty$ is the speed of sound upstream of the shock and the dimensionless time $t^* = t a_\infty/R_v$ is used. Figure 8 shows the radial sound pressure measured from the center of the vortex along the $\theta = -45^\circ$ line with respect to the $x$ axis. The results are captured at three different times for $\mathrm{Re} = 800$ and $\mathrm{Pr} = 0.75$. Compared to the DNS solution, one observes that the $D2Q9$ lattice overestimates the pressure, while removing the error terms ($\phi = 0$ and adding the correction term) leads to a significant improvement such that the latter together with the $D2Q25$ lattice are in good agreement with the DNS solution.

## V. CONCLUSION

In this paper, a consistent analysis of the particles on demand kinetic model was presented. Due to the off-lattice property of the model, the semi-Lagrangian advection is used, which requires interpolation schemes. In our Chapman-Enskog analysis, we have taken into account the effect of the interpolation and transformation of populations during the advection process. By doing so, we have derived the hydrodynamic limit of the model for commonly used one- and two-dimensional lattices. It has been demonstrated that the $D2Q9$ lattice in the PonD framework has error terms on the order of the time step in the momentum and energy equations, while the $D2Q25$ lattice can recover the full compressible NSE. However, the error terms corresponding to the energy

equation recovered from the $D2Q9$ lattice could be eliminated by adopting a second population to carry the total energy instead of the excess internal energy.

Furthermore, we discussed that similar to other semi-Lagrangian LB schemes, the spatial order of accuracy can be increased by employing high-order interpolation functions at low CFL numbers. However, the compressibility errors are no longer present thanks to the Galilean-invariant nature of the model.

As for the validation, the presented analysis were verified on various numerical benchmarks. It was shown that the results were improved upon, including corrections to remove the error terms.

Finally, we comment that the current analysis can be applied to three-dimensional lattices. In the case of tensor-product lattices such as $D3Q27$ and $D3Q125$, the recovered equations for fluid properties such as viscosity, conductivity, and Prandtl number will be the same as their two-dimensional counterparts [Eqs. (77)–(79), (84), and (89)]. However, for any general lattice, a separate investigation must be carried out due to their unique form of mapping matrix.

## ACKNOWLEDGMENTS

The author thanks I. Karlin and B. Dorschner for the discussions.

## APPENDIX

In this section, we aim to analyze the predictor-corrector step during the advection process. To this end, we take the $D1Q3$ lattice with the inverted mapping matrix $\mathcal{M}^{-1}$ as shown by Eq. (41). For simplicity, the interpolation kernel is once again neglected. The goal is to find the comoving gauge at point $x$ and time $t_0 + \delta t$ assuming that the flow variables are known at time $t_0$. As explained in Sec. III A, the particles at point $x$ are first set relative to the initial gauge $\lambda_0 = \lambda(x, t_0)$. Hence the initial values of the discrete velocities are

$$v_i^0 = v_i(x, t_0) = \sqrt{\theta_0} c_i + u_0, \tag{A1}$$

where $\theta_0 = \theta(x, t_0)$ and $u_0 = u(x, t_0)$. At the next step, the semi-Lagrangian advection is followed using Eq. (27):

$$f_i^{\lambda_0} = \mathcal{M}^{-1}_{i,\lambda_0} M^*\big(x - v_i^0 \delta t, t_0\big). \tag{A2}$$

Consequently, using Eqs. (21)–(23), the updated density, momentum, and total energy values are obtained and denoted as $\rho_1, (\rho u)_1, (2\rho E)_1$, respectively.

In general, one can express the populations at the $n$th iteration by

$$f_i^{\lambda_n} = \mathcal{M}^{-1}_{i,\lambda_n} M^*\big(x - v_i^n \delta t, t_0\big), \tag{A3}$$

where $\lambda_n = \{T_n, u_n\}$ denotes the reference frame corresponding to the computed temperature $T_n = \theta_n T_{\mathrm{L}}$ and velocity $u_n$. The flow variables are updated as

$$\rho_{n+1} = \sum_i f_i^{\lambda_n}, \tag{A4}$$

$$(\rho u)_{n+1} = \sum_i f_i^{\lambda_n} v_i^n, \tag{A5}$$

$$(2\rho E)_{n+1} = \sum_i f_i^{\lambda_n} v_i^{n2}. \tag{A6}$$

It is straightforward to show

$$\begin{aligned}
f_0^{\lambda_n} &= \left(1 - \frac{u_n^2}{\theta_n}\right)\rho(x_0^n) + \frac{2u_n}{\theta_n}(\rho u)\big(x_0^n\big) - \frac{1}{\theta_n}(2\rho E)\big(x_0^n\big), \\
f_1^{\lambda_n} &= \frac{u_n^2 - \sqrt{\theta_n} u_n}{2\theta_n}\rho\big(x_1^n\big) + \frac{\sqrt{\theta_n} - 2u_n}{2\theta_n}(\rho u)\big(x_1^n\big) \\
&\quad + \frac{1}{2\theta_n}(2\rho E)\big(x_1^n\big), \\
f_2^{\lambda_n} &= \frac{u_n^2 + \sqrt{\theta_n} u_n}{2\theta_n}\rho\big(x_2^n\big) - \frac{\sqrt{\theta_n} + 2u_n}{2\theta_n}(\rho u)\big(x_2^n\big) \\
&\quad + \frac{1}{2\theta_n}(2\rho E)\big(x_2^n\big),
\end{aligned} \tag{A7}$$

where $x_j^n$, $j = 0, 1, 2$, are the departure points as shown in Fig. 1, at the $n$th iteration, such that

$$\begin{aligned}
x_0^n &= x - u_n \delta t, \\
x_1^n &= x - \sqrt{\theta_n}\delta t - u_n \delta t, \\
x_2^n &= x + \sqrt{\theta_n}\delta t - u_n \delta t.
\end{aligned} \tag{A8}$$

It can be observed that $x_0^n$ is always the middle point between $x_1^n$ and $x_2^n$. Note that the moments $[\rho, \rho u, 2\rho E]$ in Eq. (A7)—evaluated at departure points $x_j^n$—are known from the previous time step $t = t_0$. It must be commented that the transformation process is not positivity preserving; i.e., the transformed populations can assume negative values depending on the target reference frame [see Eq. (A7)].

Before proceeding further, we use Taylor series to expand these terms around $(x, t_0)$ up to third-order accuracy. Finally, taking the first two moments of Eqs. (A7), we have

$$\rho_{n+1} = \rho(x, t_0) - \delta t \partial_x(\rho u) + \frac{\delta t^2}{2}\partial_{xx}(2\rho E) + \mathcal{O}(\delta t^3), \tag{A9}$$

$$\begin{aligned}
(\rho u)_{n+1} &= (\rho u)(x, t_0) + \frac{\delta t^2}{2} u_n^3 \partial_{xx}\rho - \frac{\delta t^2}{2} u_n \theta_n \partial_{xx}\rho \\
&\quad - \frac{3}{2}\delta t^2 u_n^2 \partial_{xx}(\rho u) + \frac{\delta t^2}{2}\theta_n \partial_{xx}(\rho u) - \delta t \partial_x(2\rho E) \\
&\quad + \frac{3}{2}\delta t^2 u_n \partial_{xx}(2\rho E).
\end{aligned} \tag{A10}$$

It is observed that the evaluated density during the iterations is independent of its previous values (there is no dependence on $\rho_n$). Hence, one can write $\rho = \rho_n = \rho_{n+1}$. For further simplification, assume the isothermal condition, i.e., $\theta_n = 1$. According to Eq. (A10), the difference of computed momenta between two subsequent iterations is

$$\begin{aligned}
\rho(u_{n+1} - u_n) &= \frac{\delta t^2}{2}\big(u_n^3 - u_{n-1}^3\big)\partial_{xx}\rho - \frac{\delta t^2}{2}(u_n - u_{n-1})\partial_{xx}\rho \\
&\quad - \frac{3}{2}\delta t^2\big(u_n^2 - u_{n-1}^2\big)\partial_{xx}(\rho u) \\
&\quad + \frac{3}{2}\delta t^2 (u_n - u_{n-1})\partial_{xx}(2\rho E).
\end{aligned} \tag{A11}$$

It is straightforward to show that

$$\left|\frac{u_{n+1}-u_n}{u_n-u_{n-1}}\right| = \mathcal{O}(\delta t^2). \tag{A12}$$

Hence, the predictor-corrector algorithm is always convergent at relatively low time steps.

Another approach is to evaluate the derivative of the iteration function. According to the fixed-point iteration method, the iterative process $x_{n+1} = \Psi(x_n)$ will be convergent if $|\Psi'(x)| < 1$ for a specified interval.

Rearranging Eq. (A11) as $u_{n+1} = \Psi(u_n)$, it can be shown that

$$\left|\frac{\partial \Psi}{\partial u}\right| = \mathcal{O}(\delta t^2). \tag{A13}$$


[1] S. Succi, *The Lattice Boltzmann Equation: For Complex States of Flowing Matter* (Oxford University Press, Oxford, UK, 2018)

[2] T. Krüger, H. Kusumaatmaja, A. Kuzmin, O. Shardt, G. Silva, and E. M. Viggen, *The Lattice Boltzmann Method: Principles and Practice* (Springer, Berlin, 2016).

[3] M. Sbragaglia, R. Benzi, L. Biferale, S. Succi, and F. Toschi, Phys. Rev. Lett. **97**, 204503 (2006).

[4] L. Biferale, P. Perlekar, M. Sbragaglia, and F. Toschi, Phys. Rev. Lett. **108**, 104502 (2012).

[5] R. Benzi, S. Chibbaro, and S. Succi, Phys. Rev. Lett. **102**, 026002 (2009).

[6] A. Mazloomi M, S. S. Chikatamarla, and I. V. Karlin, Phys. Rev. Lett. **114**, 174502 (2015).

[7] C. Kunert and J. Harting, Phys. Rev. Lett. **99**, 176001 (2007).

[8] J. Hyväluoma and J. Harting, Phys. Rev. Lett. **100**, 246001 (2008).

[9] M. Atif, P. K. Kolluru, C. Thantanapally, and S. Ansumali, Phys. Rev. Lett. **119**, 240602 (2017).

[10] B. Dorschner, F. Bösch, S. S. Chikatamarla, K. Boulouchos, and I. V. Karlin, J. Fluid Mech. **801**, 623 (2016).

[11] S. Pirozzoli, Annu. Rev. Fluid Mech. **43**, 163 (2011).

[12] D. Wilde, A. Krämer, D. Reith, and H. Foysi, Phys. Rev. E **101**, 053306 (2020).

[13] Y. Feng, P. Boivin, J. Jacob, and P. Sagaut, J. Comput. Phys. **394**, 82 (2019).

[14] N. Frapolli, S. S. Chikatamarla, and I. V. Karlin, Phys. Rev. E **92**, 061301(R) (2015).

[15] N. I. Prasianakis and I. V. Karlin, Phys. Rev. E **78**, 016704 (2008).

[16] N. Frapolli, S. S. Chikatamarla, and I. V. Karlin, Phys. Rev. Lett. **117**, 010604 (2016).

[17] N. Frapolli, S. S. Chikatamarla, and I. V. Karlin, Phys. Rev. E **93**, 063302 (2016).

[18] S. S. Chikatamarla and I. V. Karlin, Phys. Rev. Lett. **97**, 190601 (2006).

[19] B. Dorschner, F. Bösch, and I. V. Karlin, Phys. Rev. Lett. **121**, 130602 (2018).

[20] X. He and L.-S. Luo, Phys. Rev. E **56**, 6811 (1997).

[21] S. Ansumali and I. V. Karlin, Phys. Rev. Lett. **95**, 260605 (2005).

[22] P. Koumoutsakos, J. Comput. Phys. **138**, 821 (1997).

[23] W. M. van Rees, Ph.D. thesis, ETH Zurich (2014).

[24] A. Krämer, K. Küllmer, D. Reith, W. Joppich, and H. Foysi, Phys. Rev. E **95**, 023305 (2017).

[25] A. Krämer, D. Wilde, K. Küllmer, D. Reith, H. Foysi, and W. Joppich, Comput. Math. Appl. **79**, 34 (2020).

[26] O. Inoue and Y. Hattori, J. Fluid Mech. **380**, 81 (1999).